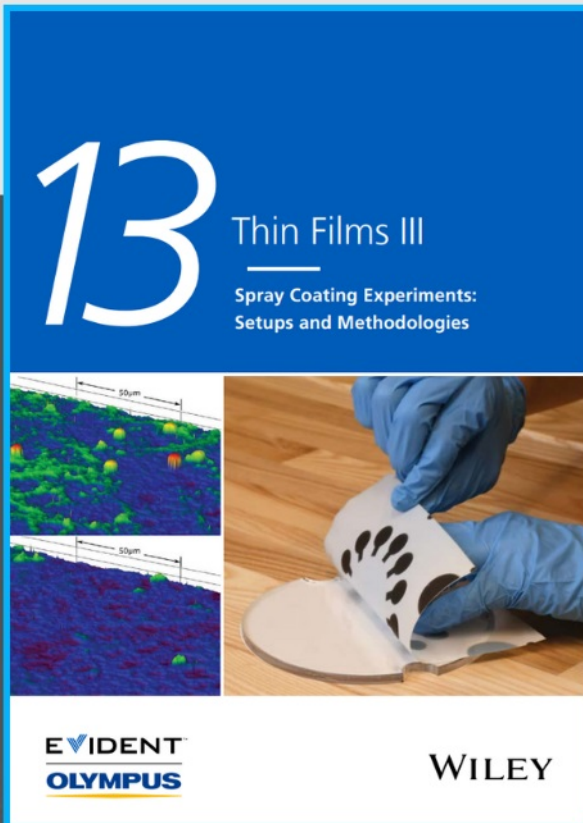




Spray Coating Experiments: Setups and Methodologies



**The latest eBook from
Advanced Optical Metrology.
Download for free.**

Spray Coating Experiments: Setups and Methodologies, is the third in our Thin Films eBook series. This publication provides an introduction to spray coating, three article digests from Wiley Online Library and the latest news about Evident's Image of the Year Award 2022.

Wiley in collaboration with Evident, are committed to bridging the gap between fundamental research and industrial applications in the field of optical metrology. We strive to do this by collecting and organizing existing information, making it more accessible and useful for researchers and practitioners alike.

EVIDENT
OLYMPUS

WILEY

Nitrogen-Doped Porous Nickel Molybdenum Phosphide Sheets for Efficient Seawater Splitting

Suraj Loomba, Muhammad Waqas Khan, Muhammad Haris, Seyed Mahdi Mousavi, Ali Zavabeti, Kai Xu, Anton Tadich, Lars Thomsen, Christopher F. McConville, Yongxiang Li, Sumeet Walia, and Nasir Mahmood*

Hydrogen is emerging as an alternative clean fuel; however, its dependency on freshwater will be a threat to a sustainable environment. Seawater, an unlimited source, can be an alternative, but its salt-rich nature causes corrosion and introduces several competing reactions, hindering its use. To overcome these, a unique catalyst composed of porous sheets of nitrogen-doped NiMo₃P (N-NiMo₃P) having a sheet size of several microns is designed. The presence of large homogenous pores in the basal plane of these sheets makes them catalytically more active and ensures faster mass transfer. The introduction of N and Ni into MoP significantly tunes the electronic density of Mo, surface chemistry, and metal-non-metal bond lengths, optimizing surface energies, creating new active sites, and increasing electrical conductivity. The presence of metal-nitrogen bonds and surface polyanions increases the stability and improves anti-corrosive properties against chlorine chemistry. Ultimately, the N-NiMo₃P sheets show remarkable performance as it only requires overpotentials of 23 and 35 mV for hydrogen evolution reaction, and it catalyzes full water splitting at 1.52 and 1.55 V to achieve 10 mA cm⁻² in 1 M KOH and seawater, respectively. Hence, structural and compositional control can make catalysts effective in realizing low-cost hydrogen directly from seawater.


1. Introduction

Hydrogen, which carries a high gravimetric energy density, has the potential to be one of the best alternatives to fossil fuels with net-zero emissions.^[1] However, the use of freshwater to produce hydrogen on a large scale is ultimately a threat to the survival of life as it puts strain on the limited freshwater reserves.^[2] On the other hand, seawater accounts for 96.5% of the world's total water resources. However, the required desalination of seawater prior to use in an electrolyzer is not only energy-intensive and costly but also leaves behind a carbon footprint. Therefore, direct electrolysis of seawater is of high importance and could be the best option for storing clean energy.^[3] However, various ionic salts and other impurities, such as microbes and small particulates, interfere with electrochemical splitting, hence making the use of seawater a challenge.^[4]

The biggest hurdle associated with seawater is the presence of chlorine anions which not only leads to chlorine evolution reaction (CER) competing with the oxygen evolution reaction (OER) on the anode but also tends to corrode the electrodes. Although chlorine is a value-added product, to meet hydrogen requirements, the resulting chlorine amount will be three to four times what the world requires (≈62 million tons/year). Hence it will be a huge challenge to dispose of all the additional chlorine.^[5] However, the thermodynamic preference of OER over CER in alkaline electrolytes can suppress the CER.^[2] But, the formation of hypochlorite at > 490 mV by chlorine interaction with OH⁻ is a challenge in attaining stable operation. Therefore, it is crucial to develop catalysts that can carry out OER at overpotentials < 490 mV to avoid the formation of hypochlorite.^[6] But the real challenge is to achieve an overall lower cell voltage due to complicated reaction kinetics for hydrogen evolution reaction (HER) over the cathode in alkaline seawater, as the extra water dissociation step (requires extra energy) is limiting the success.^[7] Therefore, highly efficient and stable catalysts need to be developed, which can catalyze both OER and HER at extremely low overpotentials to realize seawater splitting under the potential limits to avoid CER.

S. Loomba, M. W. Khan, M. Haris, S. M. Mousavi, A. Zavabeti, K. Xu, Y. Li, S. Walia, N. Mahmood
School of Engineering
RMIT University
Melbourne, VIC 3000, Australia
E-mail: nasir.mahmood@rmit.edu.au

A. Tadich, L. Thomsen
Australian Synchrotron
ANSTO, 800 Blackburn Road, Clayton, VIC 3168, Australia
C. F. McConville
Institute of Frontier Materials
Deakin University
Geelong, VIC 3216, Australia
N. Mahmood
School of Science
RMIT University
Melbourne, Victoria 3000, Australia

 The ORCID identification number(s) for the author(s) of this article can be found under <https://doi.org/10.1002/smll.202207310>.

© 2023 The Authors. Small published by Wiley-VCH GmbH. This is an open access article under the terms of the Creative Commons Attribution-NonCommercial License, which permits use, distribution and reproduction in any medium, provided the original work is properly cited and is not used for commercial purposes.

DOI: 10.1002/smll.202207310

Transition metal phosphides (TMPs) have attracted much attention in recent years due to their tuneable structure, composition, and high intrinsic catalytic activity.^[8] However, their poor stability and limited catalytic activity due to the rapid loss of active sites are the key challenges.^[9] Therefore, developing a catalyst with abundant accessible and stable active sites remains a significant challenge. It has been observed that adjusting the structure and composition of catalysts can play a crucial role in increasing the number of active sites but stabilizing them requires the appropriate engineering across each active site. For example, the unique structure of two-dimensional (2D) materials provides a large exposed surface area and a unique range of electronic properties.^[10] Traditionally, 2D materials only provide edge-exposed active sites, which no doubt play a crucial role in improving the activity, but large inert basal planes limit their full capacity.^[11] Therefore, it is necessary to make the basal plane active so it does not diminish the unique 2D features. This can be achieved by creating strain (bringing differentiated energy states) and dangling bonds as active sites by introducing defects (hetero-atoms or bond polarity) and pores. These engineered manipulations of the basal plane not only tune the active sites but also improve mass transport and conductivity.^[12] However, realizing them precisely on large area sheets of several microns and keeping them active for longer operation, especially in containments rich in corrosive seawater, is a huge challenge.

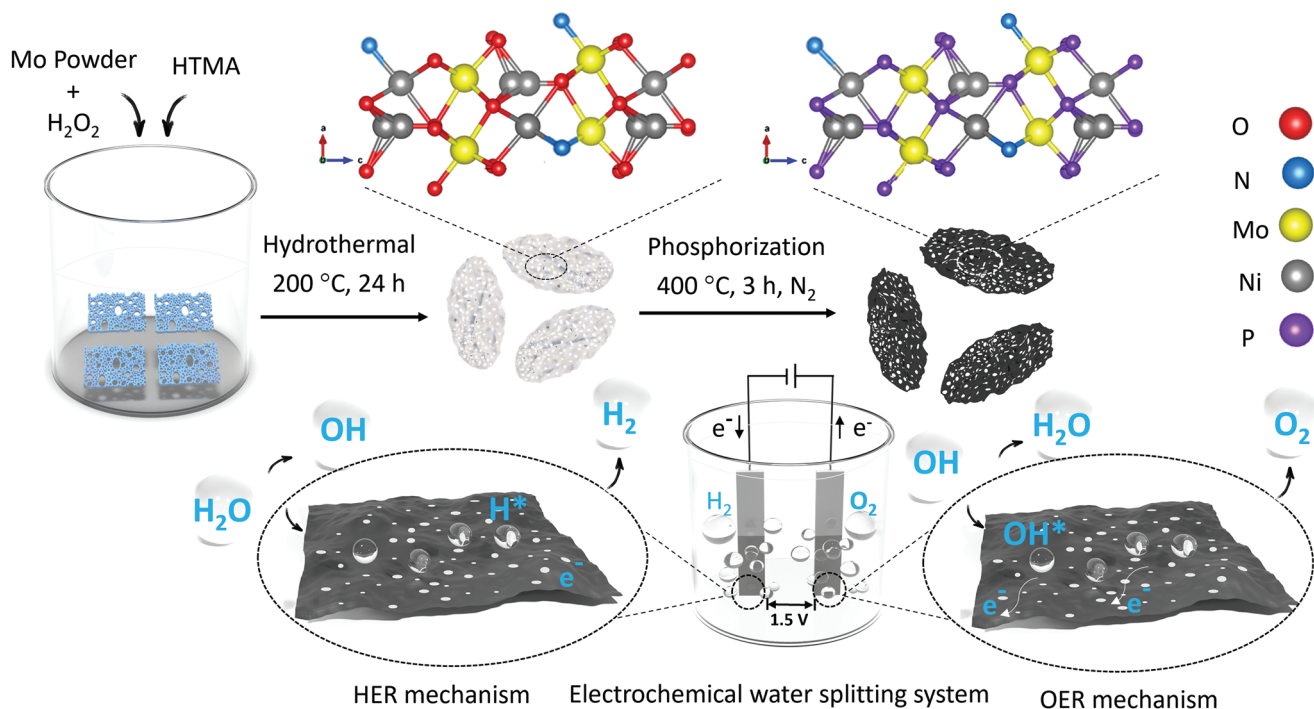
In this work, we have designed and prepared porous nitrogen-doped NiMo₃P (N-NiMo₃P) sheets of several micron sizes using a facile process. This unique catalyst has numerous active sites for efficient water catalysis as the presence of Ni and N assists in the redistribution of Mo's electron densities, enhancing the electrical conductivity and tuning the metal-non-metal bond lengths. The large homogenous pores lead to better mass transport and new active sites at the dangling bond sites of the pore edges, making the basal plane of the sheets active. The metal-nitrogen bond is responsible for the anti-corrosive properties to overcome the harsh seawater environment. The higher electronegativity of nitrogen (metal-nitrogen bonds) helps in improving the stability of active sites through the electron-withdrawing capability and helping the metal atoms to obtain a higher valence state, hence improving the transfer of electrons and mobilizing the electronic density of the catalyst. Moreover, the metal-nitrogen bond decreases the diffusion rate of any unwanted molecules/ions to the surface of the catalyst, decreasing the contact between the reactants and the seawater electrolyte.^[13] The presence of polyanions on the surface (phosphate, sulfate, and nitrate) safeguards the catalyst from chlorine chemistry.^[13] The phosphate, nitrate, and hydroxyl ions (confirmed by the FTIR and XPS analysis) make a polyanion shield to form a protective coating on the surface. The presence of these polyanions on the surface of the catalyst is known to improve the cation selectivity and tend to repel and block the chloride anions. Thus, these polyanions play a crucial role in corrosion inhibition preventing chloride anions from reaching the catalyst and corroding the underlying surface.^[13] The N-NiMo₃P sheets exhibit exceptional HER overpotential values of 23 and 35 mV at 10 mA cm⁻² in alkaline electrolytes and seawater, respectively. Besides, for full water splitting, it only requires 1.52 and 1.55 V to achieve 10 mA cm⁻² in alkaline

electrolyte and seawater, respectively. These exceptional results demonstrate that low-cost hydrogen can be generated from seawater by regulating the structure and composition of 2D materials.

2. Results and Discussion

Porous sheets of N-NiMo₃O₃ and N-NiMo₃P were synthesized via a facile hydrothermal process followed by phosphorization as an efficient catalyst for alkaline seawater splitting, as illustrated in **Scheme 1**. The nickel foam served a dual function both as a source of nickel and a template to produce porous sheets of several microns. The hexamethylenetetramine (HMTA) acts as the nitrogen source to generate an M–N bond to increase the overall electrical conductivity, intrinsic activity, and anti-corrosive properties. Intermediate annealing was carried out to remove excess oxygen and water molecules, which facilitated better phosphorization and produced a defect-rich structure by tuning the chemistry at the crystallite grain boundaries. Hence, the annealing process enriches the catalyst with active sites through grain boundary engineering and removing adsorbed species at dangling bonds present at pores and edges. This extended electrode/electrolyte interface creates a foundation for an ideal catalyst for direct seawater splitting. The impact of annealing on crystal structure modification is observed through a transmission electron microscope (TEM) imaging of as-synthesized, annealed, and phosphorized samples, as shown in Figure S1, Supporting Information. The annealing provides the required energy to re-join the small sheets to form larger sheets, introducing additional grain boundaries that will act as active sites with distinct energy differences and will be hot-spots for water adsorption and hydrogen desorption. Figure S2, Supporting Information shows scanning electron microscope (SEM) images of a) MoO₃, b) N-MoO₃, and c) N-NiMo₃O₃ without and with d) Ni foam, e) N-NiMo₃P, and f) N-NiMo₃P after testing in seawater electrolyte. The SEM images clearly show that flake-like morphology was observed without the addition of Ni, while a rod-like morphology was observed after adding Ni powder, whereas, with the addition of Ni foam, sheet-like morphology was observed. The sheet morphology was retained after phosphorization and after electrochemical testing in seawater electrolytes.

The TEM images in **Figure 1** show detailed morphological features and the texture of annealed N-NiMo₃O₃ and N-NiMo₃P sheets, where it is obvious that both samples possess ultrathin features and large lateral dimensions up to several microns. Furthermore, the TEM images clearly show the presence of homogeneously distributed pores (Figure 1b,e), indicating the formation of highly porous sheets. The existence of dangling bonds at pores creates new active sites and provides easy access through open pathways for mass transfer.^[14] The HMTA and nickel foam play a crucial role in developing such defect-rich porous sheets, as HMTA releases NH₄⁺ ions, which bind with Mo atoms and cause exfoliation and form ultrathin sheets, which upon annealing, results in nitrogen doping.^[15] The nickel foam acts as a template for the growth of porous sheets. Its inherent pore structure, under high pressure and oxidative conditions, leave its footprints; as such, no sheet formation



Scheme 1. Illustration of the synthesis of porous N-NiMo₃P and the electrochemical seawater splitting process. The porous sheets of N-NiMo₃P, owing to its large surface area with abundant active sites and pores, lead to better mass transport providing exceptional electrochemical performance in a seawater electrolyte. Note: the ball stick model is presenting the fundamental structure of oxide and phosphide not the surface chemistry of the sheet.

occurred, and pores are not observed in the absence of nickel foam (Figure S3, Supporting Information). On annealing, the loosely attached sheets connect and introduce larger grain boundaries, evident from the polycrystallinity of N-NiMo₃O₃ (the inset of Figure 1a) and N-NiMo₃P (the inset of Figure 1d) confirmed by selected area electron diffraction (SAED) results and support the observation of Figure S1, Supporting Information.

As the crystallite's edges were rich with NH₄⁺ ions, which on annealing, leave nitrogen doping at grain boundaries, making them special active sites with distinct energy to work in harsh seawater. Further, the microstructure was evaluated by conducting a high-resolution TEM (HRTEM) analysis. The lattice spacing of 0.378 nm for N-NiMo₃O₃ corresponds to the (110) plane of MoO₃ according to JCPDS No. 35-0609 (Figure 1c),

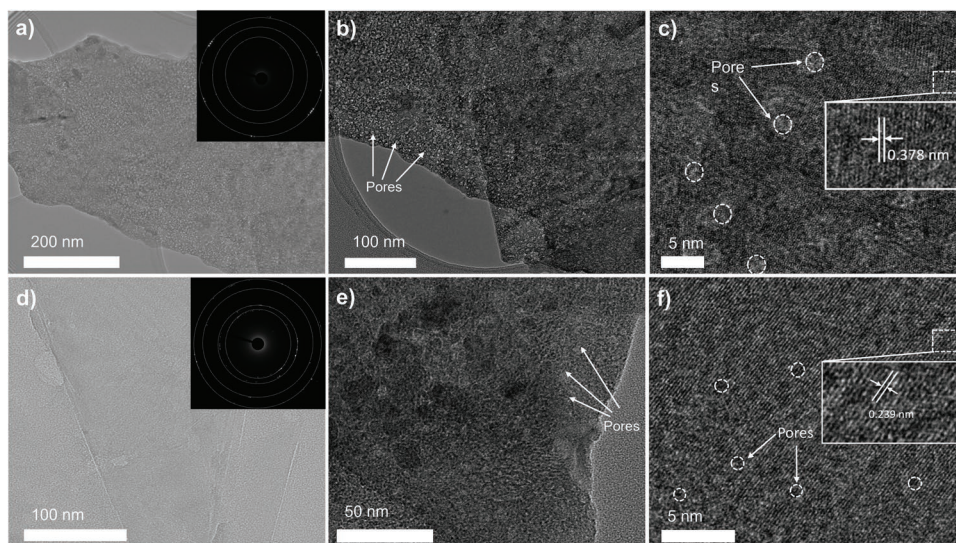


Figure 1. N-NiMo₃O₃ a) TEM image at low magnification (the inset shows SAED pattern), b) TEM image at high magnification indicating pores, and c) HRTEM showing defects and lattice spacing in the inset. N-NiMo₃P. d) TEM image at low magnification (the inset shows SAED pattern), e) TEM image at high magnification indicating pores, and f) HRTEM showing defects and lattice spacing in the inset.

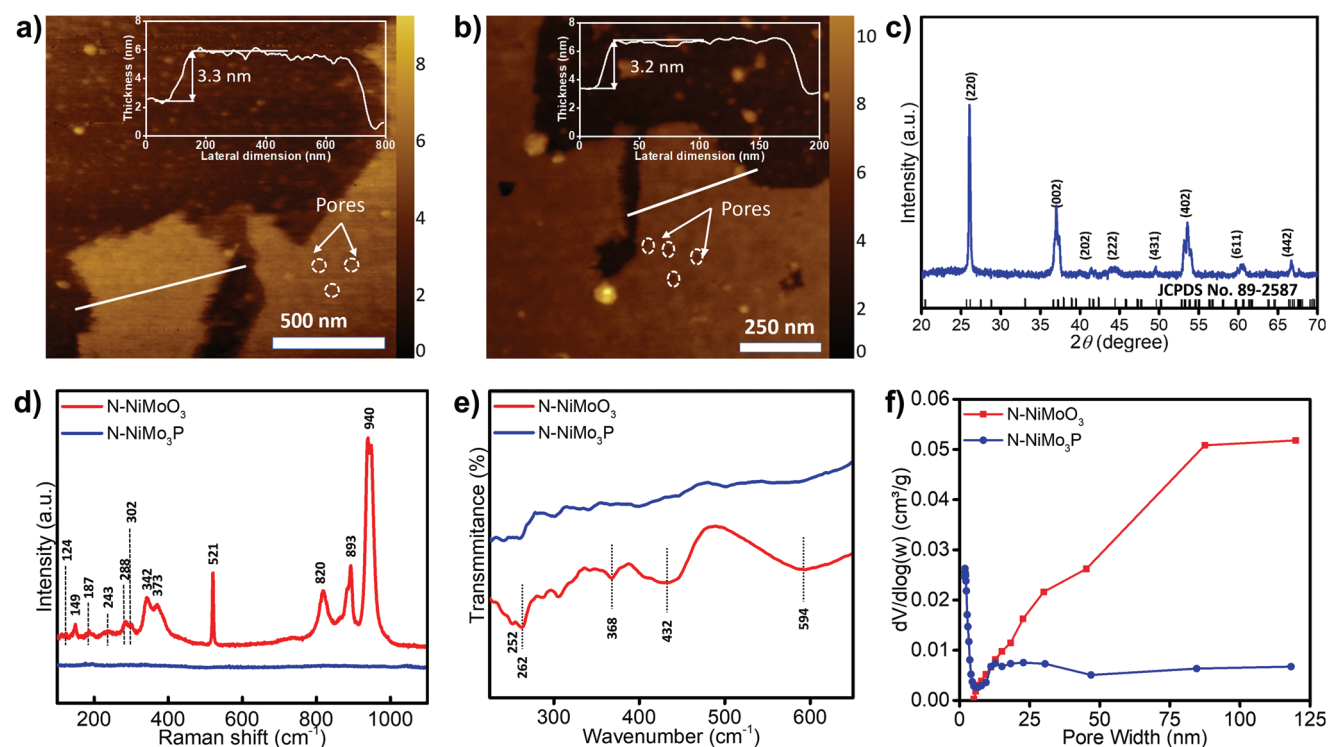


Figure 2. AFM results of cross-section topography indicating pores a) N-NiMoO₃ and b) N-NiMo₃P. The inset shows their corresponding thickness. Scan lines are shown in white. c) XRD pattern of N-NiMoO₃, N-NiMo₃P and N-NiMo₃P d) Raman spectra, e) FIR-FTIR, and f) pore volume distribution curves.

and 0.239 nm for N-NiMo₃P corresponds to the (002) plane of Mo₃P according to JCPDS No. 89–2587 (Figure 1f), confirming successful conversion to phosphide. Interestingly, the HRTEM image of both samples clearly shows the defects in the crystal structure caused by the pores and hetero-atom doping, marked by circles.

The atomic force microscope (AFM) confirmed the formation of large sheets having evidence of pores and ultrathin features of the as-synthesized sheets of N-NiMoO₃ and N-NiMo₃P, shown in Figure 2a,b, respectively. The thickness of oxide and phosphide sheets calculated using topological images are 3.3 nm (inset of Figure 2a) and 3.2 nm (inset of Figure 2b), respectively. After confirming the morphological aspects, the bulk crystal structure was analyzed using X-ray diffraction (XRD), where the pattern from N-NiMoO₃ indicates that molybdenum is the main crystal defining element, matches with the α -MoO₃ (JCPDS No. 35–0609), shown in Figure S4, Supporting Information with a small shift observed due to the introduction of N and Ni. Upon phosphorization, new peaks emerge at 26°, 37°, 41.5°, 44°, 49.5°, 53.5°, 60.5°, and 66.6°, corresponding to the crystal planes (220), (002), (202), (222), (431), (402), (611), and (442) of Mo₃P, respectively (JCPDS card No. 89–2587), without any traces of oxide (Figure 2c).

The XRD observations were further supplemented by Raman spectroscopy analysis (Figure 2d), where N-NiMoO₃ shows peaks at 243, 288, 342, 373, and 820 cm⁻¹ ascribed to α -MoO₃. A peak at 940 cm⁻¹ could be attributed to the terminal Mo=O bond stretching mode of the amorphous MoO₃ phase. This also indicates the presence of metal-oxygen bond stretching mode for

the oxide for dangling bonds. These dangling bonds are a result of the pores created during the heat treatment (Figure S5a, Supporting Information).^[16] These results again indicate that MoO₃ is the structure-defining component, as suggested by the XRD results. An average shift of 4 cm⁻¹ was observed compared to the reported values, which could well be due to the defects as a result of nitrogen doping and the addition of Ni.^[16] Interestingly, no peaks were recorded for N-NiMo₃P, confirming the successful conversion of oxide into phosphide.

Far-infrared Fourier-transform infrared spectroscopy (FIR-FTIR) measurements were carried out to analyze the surface chemistry (Figure 2e). The N-NiMoO₃ sample shows strong peaks of 432 and 594 cm⁻¹ in the spectral range of 400–650 cm⁻¹, and further peaks at \approx 252, 262, and 368 cm⁻¹ are attributed to metal-oxygen bonds.^[17] Almost all of these peaks disappeared in FIR-FTIR spectra of N-NiMo₃P, showing the successful conversion of the oxide into phosphide. Moreover, the vibrations at \approx 1258 and \approx 1634 cm⁻¹ confirm the presence of nitrate and hydroxyl groups in the N-NiMoO₃ sample (Figure S6, Supporting Information). While new peaks at \approx 400 and \approx 1038 cm⁻¹ appear in the case of N-NiMo₃P, attributing to the phosphate ion along with broader peaks at \approx 1278 and \approx 1634 cm⁻¹, indicating the presence of phosphate/nitrate and hydroxyl groups, respectively, which could be useful to protect the catalyst from anions attack (chloride present in seawater) and optimize surface for cation absorption.^[18]

Considering the highly porous nature of the as-synthesized sheets, the nitrogen adsorption/desorption isotherms were recorded, as shown in Figure S7a, Supporting Information.

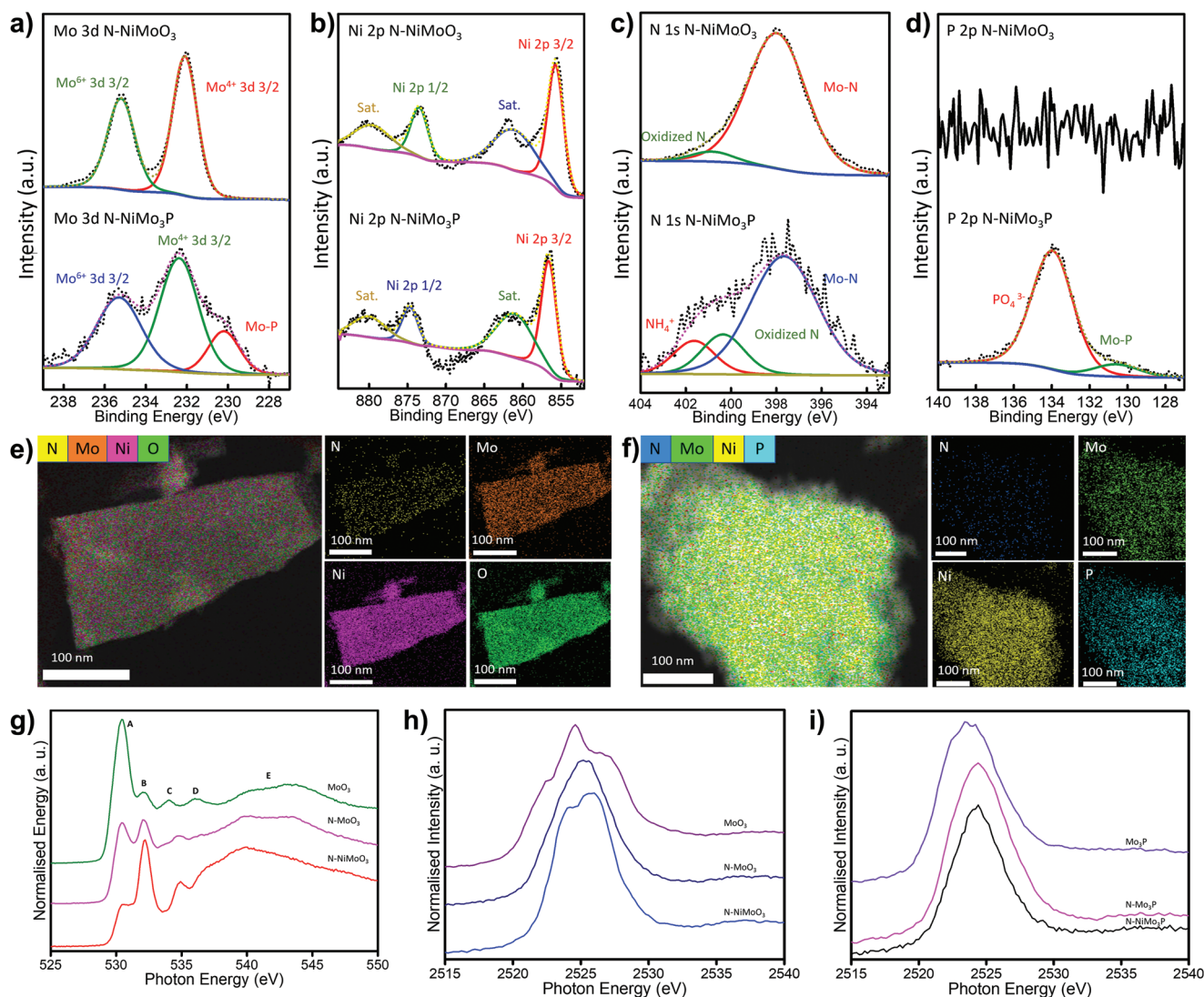


Figure 3. Deconvoluted XPS spectra of a) Mo 3d, b) Ni 2p, c) N 1s, and d) P 2p for N-NiMoO₃ and N-NiMo₃P. STEM images and EDS elemental maps of e) N-NiMoO₃ and f) N-NiMo₃P. NEXAFS spectra of g) O-K-edge of oxides, h) Mo L-edge of oxides, and i) Mo L-edge of phosphides.

Applying Brunauer–Emmett–Teller (BET) analysis, the surface areas for the oxide and phosphide were calculated to be 3.99 and 19.29 m² g⁻¹, respectively. The increased surface area after phosphorization could be attributed to the redistribution of pores from macro to meso size, as evident from the pore distribution shown in Figure 2f. The average pore diameter is decreased from 1.28 to 1.06 nm as shown by the pore size distribution curves in Figure S7b, Supporting Information; however, the pore volume is increased from 1.28 × 10⁻³ to 5.10 × 10⁻³ cm³ g⁻¹ upon oxide conversion to phosphide. It might be due to annealing which removes any unreacted compounds and helps in increasing the volume of the catalyst, and after phosphorization, the pore size decreases due to the edge reaction with phosphorus.^[19] Such mass redistribution relating to the pores means their internal structure increases the surface area and makes these pores more active and easily accessible by molecules/ions and for solvation. This contributes positively toward the material activity.

Oxidation states of the atoms within a catalyst play an important role in determining the activity and stability, which are determined by X-ray photoelectron spectroscopy (XPS). **Figure 3a** presents the Mo 3d deconvoluted spectra of both oxide and phosphide, showing two major peaks around 235.2 and 232.1 eV could be attributed to 3d_{3/2} (Mo⁶⁺) and 3d_{3/2} (Mo⁴⁺), respectively. Interestingly a new peak appears in Mo 3d after phosphorization at 230.2 eV, corresponding to the Mo-P bond in N-NiMo₃P.^[10,20] Similarly, Ni 2p deconvoluted spectra of oxide show prominent peaks around 855.7 and 873.5 eV, attributed to Ni 2p_{3/2} and Ni 2p_{1/2} and their satellites at 861.1 and 879.5 eV, respectively, showing the presence of Ni²⁺ state.^[21] However, the Ni 2p_{3/2} and Ni 2p_{1/2} peaks are shifted by 1 eV without impacting the position of the satellites in N-NiMo₃P, which could be due to metal phosphorization (Figure 3b). The deconvoluted N 1s spectra of both N-NiMoO₃ and N-NiMo₃P show the main peak around 397.8 eV, corresponding to the metal-nitrogen bond, while the oxide shows a second peak at 400.8 eV

for oxidized-N species and the phosphide shows its other peaks at 400.4 and 401.6 eV corresponding to oxidized-N species and NH_4^+ ions (Figure 3c).^[16] The deconvoluted P 2p spectrum of N-NiMo₃P reveals peaks at 130.56 and 133.9 eV, ascribing to the M-P bond, and PO_4^{3-} could be formed due to the slight surface oxidation (also observed in FTIR) (Figure 3d).^[10,20] The deconvoluted O 1s spectrum from N-NiMoO₃ shows peaks at 530.5 and 531.4 eV due to the formation of a metal-oxygen bond and oxygen in adsorbed OH group, respectively.^[15,16] The deconvoluted O 1s spectrum of phosphide has peaks at 531.14 and 532.3 eV resulting from the phosphorus-oxygen bond (phosphate) and atmospheric adsorbed oxygen (Figure S8a, Supporting Information).^[22] It is worth noting that a slight shift in the position of the peaks could be due to a redistribution of electrons created by defects, nitrogen doping, and the electronic structure's enhancement due to the synergistic effect between Ni and Mo in both systems. Hence, XPS results confirmed that Ni and N doping helps to tune the energy state of Mo as well as confirm the presence of surface phosphate and nitrates, which collectively tune the surface for efficient water catalysis and protection from corrosive chlorine chemistry.

To observe the distribution of elements across the different sheets, energy dispersive spectroscopy (EDS) elemental maps were recorded. These indicate the uniform distribution of N, Ni, Mo, and O throughout N-NiMoO₃ (Figure 3e) and N, Ni, Mo, and P throughout N-NiMo₃P (Figure 3f). These results confirm that each element is homogeneously distributed across the entire sheets, thus, helping in modulating the material's properties to achieve the maximum activity.

As XPS and EDS are surface characterization techniques, therefore, inductively coupled plasma mass spectroscopy (ICP-MS) studies were conducted to evaluate the nickel contents, which showed that the Ni is $\approx 18.4\%$ in N-NiMo₃P (Table S1, Supporting Information). Specifically, Ni and Mo were 14.2 ± 1.9 and 62.9 ± 9.9 ppb, respectively. The high concentration of Ni assures that it is not simply a dopant but a part of the structure that tunes the electron density of Mo in the d-band and modifies the energy states, creating favorable sites for water adsorption and hydrogen/oxygen desorption.

To further explain the redistribution of charge states, the regulation of electron density of the metal and non-metals involved, and the tuning of the metal-non-metal bond, near edge x-ray absorption fine structure (NEXAFS) analysis was done. Figure 3g presents the O-K-edge NEXAFS spectra of the oxide samples. The O-K-edge spectra display prominent spectral features marked A to D, corresponding to the Mo^{4+} state, while the E region corresponds to the Mo^{6+} state. It can be observed that the introduction of N and Ni in MoO₃ redistributes the electrons, as evident from the shift in photon energy around C and E and the disappearance of D. Furthermore, the dangling bonds can also be observed in the O-K-edge spectra of MoO₃, N-MoO₃, and N-NiMoO₃ represented by Figure S5b where the excitation of these energy states near the Mo^{4+} oxidation state stretching mode is in line with the metal-oxygen bond stretching mode for oxide as observed by the Raman spectroscopy results.^[23]

Figures 3h,i show the NEXAFS Mo L-edge for oxides and phosphides with and without the addition of Ni and N. It can be observed that the edge positions of Mo L-edge have

displaced to a higher photon energy after the addition of both Ni and N atoms as compared to the original MoO₃ and Mo₃P. This shift indicates that Mo in N-NiMoO₃ and N-NiMo₃P are in a higher oxidation state than that in MoO₃ and Mo₃P, respectively indicating the higher oxidation state of Mo and changes in the Mo charge density after N and Ni addition. Additionally, the d orbitals of Mo atoms tend to support the fast transfer of electrons with a low energy barrier. Due to the rapid transfer of electrons, Mo^{4+} oxidizes to Mo^{6+} , which favors the formation of more active phases during the reaction (like the oxyhydroxide phase during OER) and leads to a stronger interaction with the adsorption intermediates. Furthermore, the addition of N and Ni also makes the Mo species flexible during the oxidation-reduction cycles, which also enhances the adsorption of intermediates. Furthermore, the presence of neighboring Ni sites uplifts the d-band center of the Mo sites leading to a better transfer of electrons, and this rapid transfer of electrons is essential for improving the adsorption of intermediates and for better performance.^[24]

Although the N K-edge spectra of the N-MoO₃ and N-NiMoO₃ show very small to negligible shift in the photon energy; however, the peak in MoO₃ is broader, which means N atoms are strongly coordinated with Mo, while after the addition of Ni, the peak is less broad indicating that the bond between N and Mo weakens. This can be justified by the phosphide N K-edge spectra as well, which demonstrate the same behavior after the addition of Ni (Figure S8b, Supporting Information).^[25] These results justify that the introduction of N and Ni changes the oxidation state and hence the electron densities of Mo as well as helps in tuning the metal-non-metal bond length.

Considering the unique chemical composition and structure, as-synthesized samples were initially analyzed for HER in 1.0 M KOH and real seawater from St. Kilda beach in Melbourne, Australia. The linear sweep voltammetry (LSV) results showed that N-NiMo₃P demonstrated exceptional HER activity having low overpotentials of 23 and 35 mV to achieve a current density of 10 mA cm⁻² in 1.0 M KOH and seawater, respectively (Figure 4a). This performance is not only better than the commercial Pt/C, which required 22.5 and 73.5 mV to achieve 10 mA cm⁻² in 1.0 M KOH and seawater, respectively but also puts N-NiMo₃P among the best catalysts tested to date for direct seawater catalysis (Table S3, Supporting Information). To study the impact of nitrogen doping on the performance of the catalyst, electrochemical testing of NiMo₃P was also done. NiMo₃P required an overpotential of 61 and 73 mV in 1.0 M KOH and seawater electrolyte which is higher as compared to the overpotential required by N-NiMo₃P, indicating that nitrogen doping significantly improves the performance of the catalyst (Figure S9a, Supporting Information). However, the oxide sample did not demonstrate good HER activity as expected and required 183.5 and 218.5 mV to achieve 10 mA cm⁻² in 1.0 M KOH and seawater, respectively. This could be due to the low intrinsic affinity of oxides for HER. To understand the reaction kinetics, Tafel plots were obtained, which showed a Tafel value of 40.73 mV dec⁻¹ for N-NiMo₃P, almost the same as of Pt/C (37.51 mV dec⁻¹) in 1.0 M KOH; however, the Tafel value of our sample (44.75 mV dec⁻¹) is as low as half of Pt/C (80.45 mV dec⁻¹) in real seawater (Figure 4b). The Tafel values of oxides (578.15 and 576.56 mV dec⁻¹ in 1.0 M KOH and seawater, respectively)

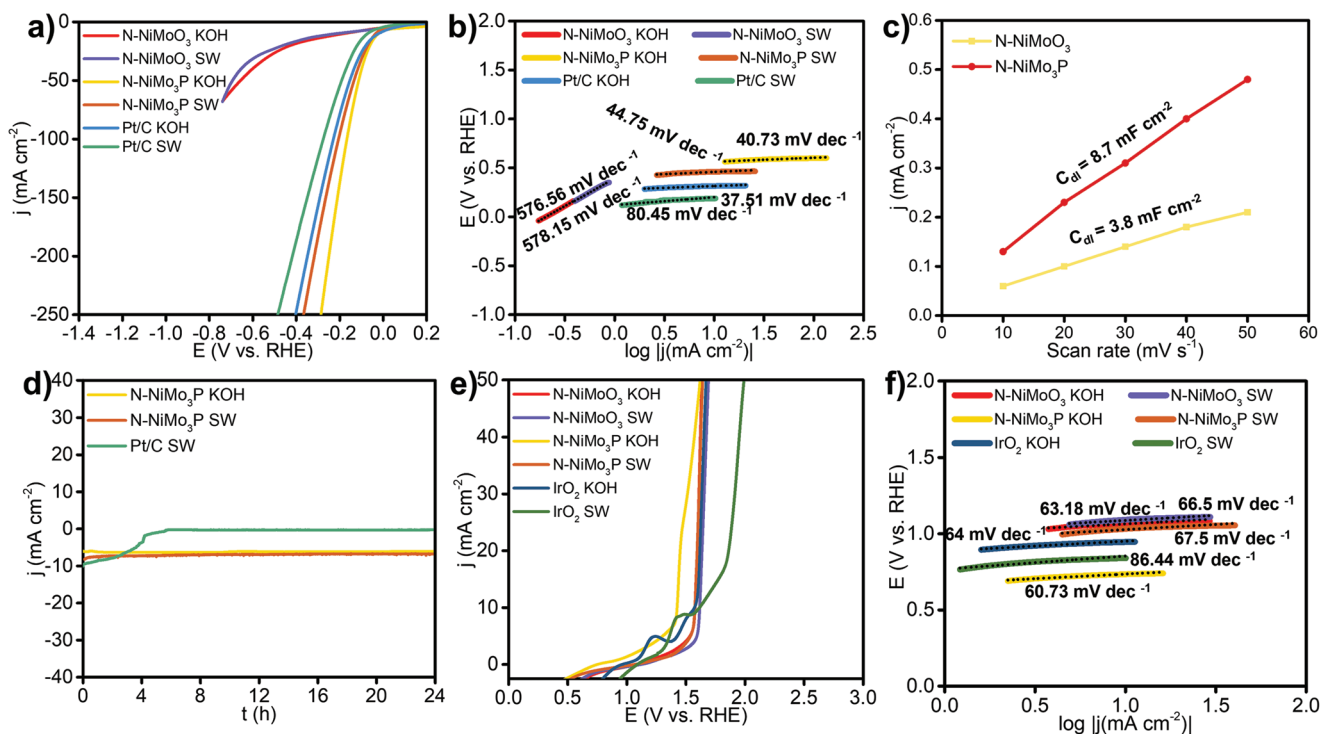


Figure 4. N-NiMo₃O₃, N-NiMo₃P, and Pt/C in 1.0 M KOH and seawater. a) Linear sweep voltammetry curves (HER) and b) corresponding Tafel plots. c) Plots showing double-layer capacitance (C_{dl}) of N-NiMo₃O₃ and N-NiMo₃P and d) current-time ($I-t$) curves of N-NiMo₃P and Pt/C for 24 h in 1.0 M KOH and seawater. N-NiMo₃O₃, N-NiMo₃P, and IrO₂ in 1.0 M KOH and seawater. e) Linear sweep voltammetry curves (OER) and f) corresponding Tafel plots. Note: All the polarization curves are iR-corrected.

were comparatively higher. Thus, proving that N-NiMo₃P bears not only low overpotentials but also shows high reaction kinetics making it a potential candidate for direct seawater splitting. This outstanding performance of N-NiMo₃P is based on its engineered composition, where the M–P bond has been altered and elongated by N doping which creates + δ and – δ charges as active hot spots to absorb the intermediates and improves the reaction kinetics by optimizing the surface energies for effective catalysis. For comparison, the overpotentials were also reported without doing IR compensation, as shown in Figure S10a, Supporting Information, and the catalyst required 29 and 41 mV to achieve 10 mA cm⁻² in 1.0 M KOH and seawater electrolyte. The electrochemical testing was also done on carbon paper electrodes to eliminate any effect of Ni foam, and the reported overpotentials for the same were 33 and 40 mV (Figure S10b, Supporting Information).

To probe the role of surface area, the electrochemical active surface was predicted by measuring the double-layer capacitance (C_{dl}) of N-NiMo₃O₃ (3.8 mF cm⁻²) and N-NiMo₃P (8.7 mF cm⁻²), which shows that phosphide has a higher active surface and support the measurements of BET analysis (Figure 4c and Figure S11, Supporting Information). This indicates the existence of abundant active sites in N-NiMo₃P, contributing to its excellent HER performance. Further, electrochemical impedance spectroscopy (EIS) was performed to understand the role of nitrogen and Ni as well as pores in improving the electrochemical performance of N-NiMo₃P (Figure S12, Supporting Information). It is observed that N-NiMo₃P faces the smallest electrolyte resistance, which is

slightly higher in seawater than in freshwater could be due to higher ionic concentration in seawater. Similarly, N-NiMo₃P also bears a smaller semi-circle than the oxide counterpart, which shows lower charge transfer resistance. These improved conductivities are due to the presence of nitrogen and nickel, which ensured enough electronic movements in the catalyst structure. Furthermore, lower Warburg (W) resistance was also observed for N-NiMo₃P, which shows faster ionic movements due to the pore-rich structure of sheets (Figure S12, Supporting Information). Hence, improved conductivities and faster mass transport contributed to the enhanced electrochemical performance of N-NiMo₃P.

Stability is one of the most critical factors in judging long-term performance; therefore, an amperometric test of N-NiMo₃P was conducted in 1.0 M KOH and real seawater. As evident from Figure 4d, the hydrogen production activity of N-NiMo₃P in 1.0 M KOH (retains 98% of its catalytic current density) and seawater (retains 82% of its catalytic current density) was exceptionally stable for 24 h. A further stability test of 100 h was also conducted in 1.0 M KOH to confirm the exceptional stability of the material, as shown in Figure S13, Supporting Information. In comparison, Pt/C has very poor stability as it retains less than 5% of its catalytic current density over the same time duration in seawater electrolyte and losses more than half of its initial current density in 1.0 M KOH (Figure 4d and Figure S14, Supporting Information). In addition, the polarization curves of the catalyst before and after 1000 cyclic voltammetry (C–V) cycles almost overlap in 1.0 M KOH (Figure S15a, Supporting Information) and seawater (Figure S15b,

Supporting Information), indicating the excellent stability of the catalyst in both electrolytes.

To be bifunctional catalysts for full water splitting, the catalysts should be capable of carrying out both anodic and cathodic reactions in the same electrolyte. Therefore, LSV curves are recorded for as-synthesized materials to evaluate their OER performance and suitability in seawater. The N-NiMo₃P delineated an exceptional OER activity, where it achieved a current density of 10 mA cm⁻² at overpotentials of only 196 and 346 mV, better than the commercial IrO₂, which required 313 and 385 mV to achieve 10 mA cm⁻² in 1.0 M KOH and seawater, respectively (Figure 4e). The impact of nitrogen doping was also studied by carrying out electrochemical testing of NiMo₃P. NiMo₃P required an overpotential of 233 and 386 mV in 1.0 M KOH and seawater electrolyte, indicating that nitrogen doping significantly improves the performance of the catalyst (Figure S9b, Supporting Information). Interestingly, it is found that after nitrogen doping the strong oxidation peaks appearing in NiMo₃P both in KOH and seawater electrolytes also disappear which signifies the role of nitrogen in improving the structural stability and inhibiting the corrosion of catalysts. Additionally, N-NiMo₃P also showed excellent OER activity, which is comparable to commercial IrO₂ as it only required overpotentials of 343 and 386 mV in 1.0 M KOH and seawater to achieve 10 mA cm⁻², respectively. More importantly, the overpotential required by N-NiMo₃P in seawater is significantly smaller than the 490 mV overpotential required to initiate the CER and thus prevent the formation of hypochlorite, where surface modification by polyanions will further assist in avoiding CER. As it has been reported that polyanions with moderate ionic potential such as phosphate ions are highly favorable to repel the chloride ions without impacting the active sites and protect the catalyst surface from corrosion and favor the adsorption of water molecules and promote the reaction kinetics.^[13] To further prove that there was no CER at the anode, electrochemical testing was done continuously to generate gas over the working electrode, which was then passed through acetone at room temperature. The reaction between chlorine gas and acetone is instantaneous and gives chloroacetone and HCl. The chlorine reacts quantitatively with acetone with zero concentration of chlorine at the outlet.^[26] However, when the gas collected from the cell was passed through acetone, no such reaction was observed, confirmed qualitatively by the pH test of the solution (Figure S16a, Supporting Information). For further quantitative confirmation of chlorine selectivity, a gas chromatograph mass spectrometer (GC-MS) was used to analyze the acetone + gas mixture. Figure S16b, Supporting Information shows that the peaks obtained after the GC-MS of the solvent correspond majorly to acetone except for the sharp peak around 6, which attributes to the internal standard peak. Hence, confirming that chlorine was not generated at the anode as no signals were found for chloroacetone, and developed catalysts show high selectivity towards OER and have the ability to suppress the CER, hence making it suitable for seawater catalysis.^[27]

Further, a much lower Tafel value of 67.5 mV dec⁻¹ for N-NiMo₃P than IrO₂ (86.44 mV dec⁻¹) in real seawater shows its superior reaction kinetics (Figure 4f). The same trend is observed for Tafel values in an alkaline electrolyte where N-NiMo₃P (60.73 mV dec⁻¹) is performing better than IrO₂

(64 mV dec⁻¹). Interestingly, N-NiMo₃P also showed better Tafel values (63.18 and 66.5 mV dec⁻¹ in 1.0 M KOH and seawater, respectively) than that of standard IrO₂. Hence, proving that structural and morphological maneuvering of materials are highly beneficial in attaining efficient catalysis at low overpotentials.

Finally, N-NiMo₃P was used as both the anode and cathode to carry out full water splitting in 1.0 M KOH and real seawater in a two-electrode system to explore its commercial applicability. The LSV curves of N-NiMo₃P || N-NiMo₃P show an exceptional performance by achieving a current density of 10 mA cm⁻² at low total cell voltages of 1.52 and 1.55 V in 1.0 M KOH and seawater, respectively (Figure 5a). This performance is not only better than the coupled benchmark Pt/C || IrO₂ full cell that required a cell voltage of 1.584 and 1.607 V to achieve 10 mA cm⁻² in 1.0 M KOH and seawater, respectively but also the best among the reported catalysts (Table S4, Supporting Information). The Tafel plots further demonstrate much better reaction kinetics of N-NiMo₃P || N-NiMo₃P (Tafel value of 53.59 and 65.86 mV dec⁻¹) than the coupled Pt/C || IrO₂ (66.11 and 71.24 mV dec⁻¹) both in 1.0 M KOH and real seawater, respectively (Figure 5b). To evaluate the long-term performance of the catalyst, an amperometric test of the N-NiMo₃P was conducted, where it retained 87% (1.0 M KOH) and 86% (seawater) of its catalytic current density for 24 h (Figure 5c). In comparison, coupled Pt/C || IrO₂ system showed very poor stability by retaining only < 5% of its catalytic current density over the same time duration (Figure 5c and Figure S17, Supporting Information).

This exceptional electrochemical performance of N-NiMo₃P is based on its unique composition, structure, morphology, and surface chemistry, which play key roles such as: i) N-doping manipulated the surface energy through tuning the metal-non-metal bond; ii) accelerated charge transfer and electronic redistribution of Mo by Ni (presence of N multiply the effect) making it more susceptible for H₂O adsorption and H₂ desorption; iii) negatively charged surface polyanions tune the surface energy for proton adsorption and more importantly act as repellent for chloride ions; iv) homogenous pores across the entire sheet assuring high mass transfer and introducing new active sites through dangling bonds present at pores; v) existence of large number of grain boundaries at the connecting point of crystallites to form large sheets and strain act as binding and active sites; and vi) finally the N-doping effectively stabilize the structure and regulate the intrinsic electroactive sites to promote the catalysis. All these features have been controlled with great care in the developed catalysts, and the resulting electrochemical response has proved their benefits; however, for long-term operations, these features should be stable with ongoing electrochemical activity on catalysts in the presence of harsh solvents. To monitor the preservation of the aforementioned features, a set of ex situ characterizations have been utilized, such as XRD, TEM, Raman spectroscopy, STEM-EDS, ICP-MS, and XPS, after a continuous operation of 24 h.

It is worth mentioning that the XRD of the electrode after HER testing (which is more susceptible for metal depositions) in seawater electrolyte demonstrated the same peaks (well-matched with standard JCPDS card No. 89-2587) as observed for the as-synthesized N-NiMo₃P, shown in Figure S18,

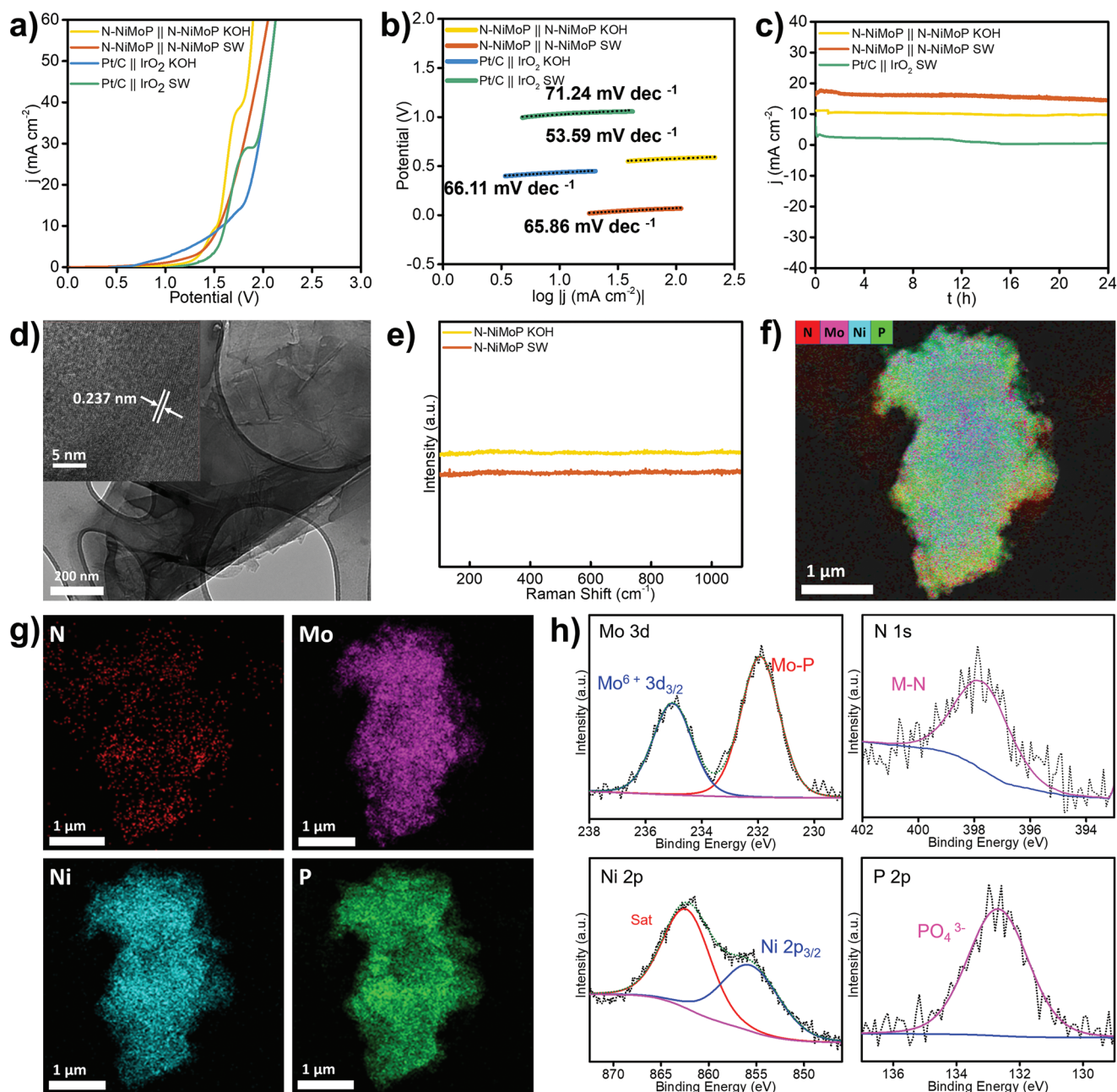


Figure 5. N-NiMo₃P || N-NiMo₃P and Pt/C || IrO₂ in 1.0 M KOH and seawater. a) Polarization curves, b) corresponding Tafel plots and c) current-time (*I*-*t*) curves for 24 h. Ex situ characterization of N-NiMo₃P after electrochemical testing in seawater. d) TEM image (HRTEM in the inset), e) Raman Spectra, f) STEM image, g) EDS elemental maps, and h) deconvoluted XPS spectra of Mo 3d, Ni 2p, N 1s, and P 2p.

Supporting Information. The XRD results indicated that there was no deposition of any foreign materials, which demonstrates that the impurities present in seawater do not impact the catalyst performance, and the structure of the catalyst was retained, which was also confirmed by the TEM results. The TEM image recorded after 24 h of operation clearly shows ultrathin 2D features without any lateral size reduction of N-NiMo₃P, confirming the material's high morphological and structural stability even in a harsh seawater environment (Figure 5d). This also confirms that grain boundaries remain connected to keep the crystallite unified and active sites alive,

as well as no material degradation occurs at the pore openings, which are generally more susceptible to a corrosive environment. Further, high structural stability also reveals that no CER and hypochlorite formation occurs, and catalysts are stable to accommodate any such minute product formation due to their unique surface chemistry and surface protection by negatively charged polyanions. Furthermore, Raman spectroscopy analysis also confirmed structural stability as no excessive oxidation of N-NiMo₃P is observed, which shows that controlled composition provides high phase stability (Figure 5e). Interestingly, EDS analysis (Figures 5f,g) demonstrates the homogenous

distribution of N, Mo, Ni, and P over the catalyst, and no deposition of Mg or Ca ions on the catalyst surface is observed, confirming its high selectivity towards proton and no parasitic attack of metal cations, hence supporting exceptional long-term stable operation of catalyst in seawater. Figure S19, Supporting Information shows the elemental map of a thin oxygen layer that may be aroused from phosphorus-oxygen or nitrogen-oxygen species on the surface of the sample or due to the surface oxidation/adsorbed oxygen.

Considering the limitation of EDS, we conducted an ICP-MS analysis of the used catalyst which showed that no metals were deposited and the ratio of Ni/Mo in the catalyst remained the same (Table S2, Supporting Information). Figure 5h shows the ex situ XPS high-resolution spectra of Mo, Ni, P, and N for N-NiMo₃P. The Mo 3d deconvoluted spectra show two major peaks at 235 and 231.9 eV ascribing to a high oxidation state Mo⁶⁺ 3d_{3/2} and Mo-P bond; the existence of a high oxidation state and Mo-P make Mo a favorable site for catalysis. The Ni 2p deconvoluted spectra show two peaks at 855.6 and 862.3 eV that ascribe to the Ni 2p_{3/2} and its satellite, indicating the presence of Ni²⁺ state and no change occurred in its oxidation states showing Ni is continuously playing a role in stabilizing Mo active sites. The deconvoluted N 1s XPS spectra show a peak around 397.69 eV, attributed to the metal-nitrogen bond, which is crucial for providing anti-corrosive properties to the catalyst for continuous catalysis over a long time. The deconvoluted P 2p spectra of the sample show peak at 132.68 eV attributed to surface oxidation to yield phosphate species which act as a stabilizer against chlorine chemistry in conjunction with nitrate polyanions. The deconvoluted O 1s spectrum shows a peak at 531.14 eV arising from a phosphorus-oxygen bond (Figure S20, Supporting Information).^[22] The small shift in the peak positions remained the same as of original results, that is, due to the electron redistribution by defects, nitrogen doping, and the enhancement of electronic structure by Ni. Overall, these results strongly demonstrate that the catalyst's composition, surface, structure, and morphology remain intact, indicating its exceptional stability and performance in carrying out direct seawater catalysis.

3. Conclusion

In summary, we have developed a facile method to prepare and engineer porous sheets of N-NiMo₃P through thermally assisted wet chemistry. The resulting large area sheets containing Ni and N dopants assist in the redistribution of electronic densities of Mo, tuning metal-non-metal bond lengths, and enhancing electrical conductivity. This creates a unique catalyst that has significantly increased active sites for efficient water catalysis. The porous structure of the sheets not only allows faster mass transport but also introduces additional active sites at dangling bond sites at the pore edges, making the entire basal plane of large N-NiMo₃P sheets active. The presence of a metal-nitrogen bond provides anti-corrosive properties to the catalyst to tackle the harsh seawater environment, while the existence of surface polyanions (phosphate and nitrate) protects the catalyst against chlorine chemistry. As a result, the catalyst shows exceptional performance by achieving the current density of 10 mA cm⁻² at low overpotentials of 23 and 35 mV for HER in 1.0 M KOH and

seawater, respectively. Furthermore, the catalysts only required the total cell voltages of 1.52 and 1.55 V to achieve the current density of 10 mA cm⁻² when used both as an anode and cathode for overall water splitting in alkaline electrolytes and seawater. Further, GC-MS analysis showed that as-synthesized catalyst showed high selectivity towards OER with complete suppression of CER. Hence, this work demonstrates a simple strategy to synthesize highly effective catalysts for direct seawater electrolysis, which is crucial in reducing the strain on freshwater resources and avoiding the energy-intensive and carbon-emitting desalination process.

4. Experimental Section

Synthesis of Nitrogen-Doped Nickel Molybdenum Phosphide: To prepare N-NiMo₃P, a sacrificial N-NiMoO₃ sample was first synthesized by a facile hydrothermal process. In detail, 500 mg of Mo powder was taken in a 20 mL glass vial to which 6 mL of 30% w/w hydrogen peroxide was added dropwise, leading to an exothermic reaction forming a yellow colored peroxomolybdic solution. In another 20 mL glass vial, 350 mg of hexamethylenetetramine (HMTA) (nitrogen source) was added to 10 mL deionized (DI) water and mixed well to obtain a transparent solution. Following this, 320 mg of Ni foam was added to the peroxomolybdic solution along with the slow addition of the HMTA solution under continuous stirring for 30 min. The solution was transferred to a Teflon-lined stainless-steel autoclave, and a hydrothermal reaction was carried out at a temperature of 200 °C for 24 h, then cooled naturally to room temperature. The sample was washed twice with DI water and ethanol, and the resulting powder sample was dried overnight in a vacuum oven at 40 °C. The dried sample was then annealed in a tube furnace under continuous nitrogen flow at a temperature of 350 °C for 2 h at the heating rate of 3 °C min⁻¹. Finally, the sample was phosphorized at 400 °C with a heating rate of 3 °C min⁻¹ under a nitrogen atmosphere for 3 h. Sodium hypophosphite was used as the phosphorus source while keeping the ratio between the sample and the P source at 1:30. Details of the materials characterization and electrochemical testing (both in an alkaline electrolyte and seawater) are provided in the Supporting Information.

Supporting Information

Supporting Information is available from the Wiley Online Library or from the author.

Acknowledgements

The authors would like to acknowledge access to the RMIT Micro Nano Research Facility (MNRF) in the Victorian node of the Australian National Fabrication Facility (ANFF), the RMIT Microscopy and Microanalysis Facility (RMMF), as well as the financial support from the Vice-Chancellor fellowship scheme at RMIT University. The authors would like to acknowledge the Australian Synchrotron, ANSTO facility in Melbourne, Victoria as "part of this research was undertaken on the soft X-ray beamline at the Australian Synchrotron," part of ANSTO. Open access publishing facilitated by RMIT University, as part of the Wiley - RMIT University agreement via the Council of Australian University Librarians.

Conflict of Interest

The authors declare no conflict of interest.

Data Availability Statement

The data that support the findings of this study are available from the corresponding author upon reasonable request.

Keywords

2D, chlorine and hydrogen evolution reaction, molybdenum phosphide, oxygen evolution reaction, seawater splitting

Received: November 23, 2022

Revised: December 9, 2022

Published online:

- [1] a) J. Wang, Y. Gao, H. Kong, J. Kim, S. Choi, F. Ciucci, Y. Hao, S. Yang, Z. Shao, J. Lim, *Chem. Soc. Rev.* **2020**, *49*, 9154; b) L. N. Chen, K. P. Hou, Y. S. Liu, Z. Y. Qi, Q. Zheng, Y. H. Lu, J. Y. Chen, J. L. Chen, C. W. Pao, S. B. Wang, Y. B. Li, S. H. Xie, F. D. Liu, D. Prendergast, L. E. Klebanoff, V. Stavila, M. D. Allendorf, J. Guo, L. S. Zheng, J. Su, G. A. Somorjai, *J. Am. Chem. Soc.* **2019**, *141*, 17995.
- [2] L. Yu, Q. Zhu, S. Song, B. McElhenny, D. Wang, C. Wu, Z. Qin, J. Bao, Y. Yu, S. Chen, Z. Ren, *Nat. Commun.* **2019**, *10*, 5106.
- [3] a) L. Yu, L. Wu, S. Song, B. McElhenny, F. Zhang, S. Chen, Z. Ren, *ACS Energy Lett.* **2020**, *5*, 2681; b) W. Tong, M. Forster, F. Dionigi, S. Drespf, R. Sadeghi Erami, P. Strasser, A. J. Cowan, P. Farràs, *Nat. Energy* **2020**, *5*, 367.
- [4] a) L. Yu, L. Wu, B. McElhenny, S. Song, D. Luo, F. Zhang, Y. Yu, S. Chen, Z. Ren, *Energy Environ. Sci.* **2020**, *13*, 3439; b) X. Wu, S. Zhou, Z. Wang, J. Liu, W. Pei, P. Yang, J. Zhao, J. Qiu, *Adv. Energy Mater.* **2019**, *9*, 1901333.
- [5] Y. Kuang, M. J. Kenney, Y. Meng, W. H. Hung, Y. Liu, J. E. Huang, R. Prasanna, P. Li, Y. Li, L. Wang, M. C. Lin, M. D. McGehee, X. Sun, H. Dai, *Proc. Natl. Acad. Sci. U. S. A.* **2019**, *116*, 6624.
- [6] a) J. Chang, G. Wang, Z. Yang, B. Li, Q. Wang, R. Kuliiev, N. Orlovskaya, M. Gu, Y. Du, G. Wang, Y. Yang, *Adv. Mater.* **2021**, *33*, 2101425; b) F. Sun, J. Qin, Z. Wang, M. Yu, X. Wu, X. Sun, J. Qiu, *Nat. Commun.* **2021**, *12*, 4182.
- [7] H. Q. Fu, M. Zhou, P. F. Liu, P. Liu, H. Yin, K. Z. Sun, H. G. Yang, M. Al-Mamun, P. Hu, H. F. Wang, H. Zhao, *J. Am. Chem. Soc.* **2022**, *144*, 6028.
- [8] L. Wu, F. Zhang, S. Song, M. Ning, Q. Zhu, J. Zhou, G. Gao, Z. Chen, Q. Zhou, X. Xing, T. Tong, Y. Yao, J. Bao, L. Yu, S. Chen, Z. Ren, *Adv. Mater.* **2022**, *34*, 2201774.
- [9] D. Zhao, R. Zhao, S. Dong, X. Miao, Z. Zhang, C. Wang, L. Yin, *Energy Environ. Sci.* **2019**, *12*, 2422.
- [10] Y. Gu, A. Wu, Y. Jiao, H. Zheng, X. Wang, Y. Xie, L. Wang, C. Tian, H. Fu, *Angew. Chem., Int. Ed.* **2021**, *60*, 6673.
- [11] X. Jin, T.-H. Gu, K.-G. Lee, M. J. Kim, M. S. Islam, S.-J. Hwang, *Coord. Chem. Rev.* **2020**, *415*, 213280.
- [12] a) X. Gong, J. Zhu, J. Li, R. Gao, Q. Zhou, Z. Zhang, H. Dou, L. Zhao, X. Sui, J. Cai, Y. Zhang, B. Liu, Y. Hu, A. Yu, S. h. Sun, Z. Wang, Z. Chen, *Adv. Funct. Mater.* **2020**, *31*, 2008085; b) D. Luo, C. Ma, J. Hou, Z. Zhang, R. Feng, L. Yang, X. Zhang, H. Lu, J. Liu, Y. Li, Y. Zhang, X. Wang, Z. Chen, *Adv. Energy Mater.* **2022**, *12*, 2103716; c) H. Huang, A. Cho, S. Kim, H. Jun, A. Lee, J. W. Han, J. Lee, *Adv. Funct. Mater.* **2020**, *30*, 2003889.
- [13] a) B. E. A. Rani, B. B. J. Basu, *Int. J. Corros.* **2012**, *2012*, 380217; b) R. Jamil, R. Ali, S. Loomba, J. Xian, M. Yousaf, K. Khan, B. Shabbir, C. F. McConville, A. Mahmood, N. Mahmood, *Chem. Catal.* **2021**, *1*, 802; c) H.-Y. Wang, J.-T. Ren, L. Wang, M.-L. Sun, H.-M. Yang, X.-W. Lv, Z.-Y. Yuan, *J. Energy Chem.* **2022**, *75*, 66; d) M. Yu, J. Li, F. Liu, J. Liu, W. Xu, H. Hu, X. Chen, W. Wang, F. Cheng, *J. Energy Chem.* **2022**, *72*, 361.
- [14] H. Chen, X. Liang, Y. Liu, X. Ai, T. Asefa, X. Zou, *Adv. Mater.* **2020**, *32*, 2002435.
- [15] F. Haque, A. Zavabeti, B. Y. Zhang, R. S. Datta, Y. Yin, Z. Yi, Y. Wang, N. Mahmood, N. Pillai, N. Syed, H. Khan, A. Jannat, N. Wang, N. Medhekar, K. Kalantar-zadeh, J. Z. Ou, *J. Mater. Chem. A* **2019**, *7*, 257.
- [16] a) P. Basu, K. Mukherjee, S. Khamrui, S. Mukherjee, M. Ahmed, K. Acharya, D. Banerjee, P. M. G. Nambissan, K. Chatterjee, *Mater. Adv.* **2020**, *1*, 1726; b) B. Maté, M. Á. Satorre, R. Escribano, *Phys. Chem. Chem. Phys.* **2021**, *23*, 9532.
- [17] a) G. A. Nazri, C. Julien, *Solid State Ionics* **1992**, *53–56*, 376; b) Z. Lin, C. Du, B. Yan, C. Wang, G. Yang, *Nat. Commun.* **2018**, *9*, 4036; c) M. W. Khan, B. Y. Zhang, K. Xu, M. Mohiuddin, A. Jannat, F. Haque, T. Alkathiri, N. Pillai, Y. Wang, S. Z. Reza, J. Li, X. Mulet, R. Babarao, N. Mahmood, J. Z. Ou, *J. Colloid Interface Sci.* **2021**, *588*, 305.
- [18] a) P. K. Verma, P. K. Mohapatra, A. Bhattacharyya, A. K. Yadav, S. N. Jha, D. Bhattacharyya, *New J. Chem.* **2018**, *42*, 5243; b) A. Chatterjee, S. Majumdar, A. Ghosh, *Solid State Ionics* **2020**, *347*, 115238; c) R. Rajagopalan, L. Zhang, S. X. Dou, H. Liu, *Adv. Energy Mater.* **2016**, *6*, 1501760.
- [19] H. Zhou, M. Zheng, H. Pang, *J. Chem. Eng.* **2021**, *416*, 127884.
- [20] P. Xiao, M. A. Sk, L. Thia, X. Ge, R. J. Lim, J.-Y. Wang, K. H. Lim, X. Wang, *Energy Environ. Sci.* **2014**, *7*, 2624.
- [21] a) L. Wang, J. Fan, Y. Liu, M. Chen, Y. Lin, H. Bi, B. Liu, N. Shi, D. Xu, J. Bao, M. Han, *Adv. Funct. Mater.* **2021**, *31*, 2010912; b) C. Liao, B. Yang, N. Zhang, M. Liu, G. Chen, X. Jiang, G. Chen, J. Yang, X. Liu, T. S. Chan, Y. J. Lu, R. Ma, W. Zhou, *Adv. Funct. Mater.* **2019**, *29*, 1904020.
- [22] V. Sydorchuk, O. I. Poddubnaya, M. M. Tsyba, O. Zakutevskyy, O. Khyzhun, S. Khalameida, A. M. Puziy, *Appl. Surf. Sci.* **2021**, *535*, 147667.
- [23] a) P. Thakur, J. C. Cezar, N. B. Brookes, R. J. Choudhary, D. M. Phase, K. H. Chae, R. Kumar, *Hyperfine Interact.* **2010**, *197*, 95; b) P. Parent, C. Laffon, *J. Chem. Phys.* **2002**, *117*, 10842; c) J. Diaz, O. R. Monteiro, Z. Hussain, *Phys. Rev. B* **2007**, *76*, 094201.
- [24] a) S. T. Oyama, P. Clark, V. L. S. Teixeira da Silva, E. J. Lede, F. G. Requejo, *J. Phys. Chem. B* **2001**, *105*, 4961; b) H. Jiang, M. Sun, S. Wu, B. Huang, C.-S. Lee, W. Zhang, *Adv. Funct. Mater.* **2021**, *31*, 2104951; c) J. Gao, C.-Q. Xu, S.-F. Hung, W. Liu, W. Cai, Z. Zeng, C. Jia, H. M. Chen, H. Xiao, J. Li, Y. Huang, B. Liu, *J. Am. Chem. Soc.* **2019**, *141*, 3014; d) R. Zhang, Y.-C. Zhang, L. Pan, G.-Q. Shen, N. Mahmood, Y.-H. Ma, Y. Shi, W. Jia, L. Wang, X. Zhang, W. Xu, J.-J. Zou, *ACS Catal.* **2018**, *8*, 3803.
- [25] J. Yang, B. Chen, X. Liu, W. Liu, Z. Li, J. Dong, W. Chen, W. Yan, T. Yao, X. Duan, Y. Wu, Y. Li, *Angew. Chem., Int. Ed.* **2018**, *130*, 9639.
- [26] a) J. P. Guthrie, J. Cossar, *Can. J. Chem.* **1986**, *64*, 1250; b) J. Markoš, L. Jelemský, M. Šóoš, V. Čamaj, *Chem. Pap.* **1999**, *53*, 349.
- [27] a) R. L. Cordell, H. Pandya, M. Hubbard, M. A. Turner, P. S. Monks, *Anal. Bioanal. Chem.* **2013**, *405*, 4139; b) K. Lakshmanan, M. Arumugam, *Asian J. Pharm. Clin. Res.* **2017**, *10*, 109.